This document is downloaded from DR-NTU (https://dr.ntu.edu.sg)
Nanyang Technological University, Singapore.

Synthesis and crystal chemistry of the hybrid perovskite (CH3NH3)PbI3 for solid-state sensitised solar cell applications

Baikie, Tom; Fang, Yanan; Kadro, Jeannette M.; Schreyer, Martin K.; Wei, Fengxia; Mhaisalkar, Subodh Gautam; Graetzel, Michael; White, Timothy John

2013

Baikie, T., Fang, Y., Kadro, J. M., Schreyer, M. K., Wei, F., Mhaisalkar, S. G., Graetzel, M.,& White, T. J. (2013). Synthesis and crystal chemistry of the hybrid perovskite (CH3NH3)PbI3 for solid-state sensitised solar cell applications. Journal of materials chemistry A, 1(18), 5628- 5641.

https://hdl.handle.net/10356/100342

https://doi.org/10.1039/c3ta10518k

© 2013 Royal Society of Chemistry. This is the author created version of a work that has been peer reviewed and accepted for publication by Journal of Materials Chemistry A , Royal Society of Chemistry. It incorporates referee’s comments but changes resulting from the publishing process, such as copyediting, structural formatting, may not be reflected in this document. The published version is available at: http://dx.doi.org/10.1039/c3ta10518k.

Downloaded on 23 Aug 2022 22:08:58 SGT

Synthesis and crystal chemistry of the hybrid perovskite $(CH_3NH_3)PbI_3$ for solid-state sensitised solar cell applications

Tom Baikie,[1]* Yanan Fang,[1] Jeannette M. Kadro,[1] Martin Schreyer,[2] Fengxia Wei,[3] Subodh Mhaisalkar,[1] Michael Graetzel,[4] Tim J. White[3]

1 Energy Research Institute @ NTU (ERI@N), Research Technoplaza, Nanyang Technological University, Nanyang Drive, 637553, Singapore.

2 Institute of Chemical Engineering Sciences, 1 Pesek Road, Jurong Island, 627833, Singapore.

3 School of Materials Science and Engineering, Nanyang Technological University, Nanyang Avenue, 639798, Singapore.

4 Laboratory for Photonics and Interfaces, Institute of Chemical Sciences and Engineering, School of Basic Sciences, Ecole Polytechnique Fédérale de Lausanne, CH-1015 Lausanne, Switzerland.

*Corresponding author – tbaikie@ntu.edu.sg

Abstract

The hybrid organic-inorganic perovskite $(CH_3NH_3)PbI_3$ may find application in next generation solid-state sensitised solar cells. Although this material and related perovskites were discovered many decades ago, questions remain concerning their diverse structural chemistry and unusual properties. The article presents a review of previous work and provides a detailed description of the preparation, structural characterisation and physical characteristics of $(CH_3NH_3)PbI_3$. The phase changes exhibited by $(CH_3NH_3)PbI_3$ have been probed using variable temperature powder and single crystal X-ray diffraction, combined with differential scanning calorimetry, thermogravimetic analysis and phase contrast transmission electron microscopy. The optical band gap for $(CH_3NH_3)PbI_3$ determined by UV-Visible spectroscopy was compared to values obtained from density-of-state simulation of electronic band structure.

1. Introduction

Recent reports of high conversion efficiencies (> 9%) for solid-state sensitised solar cell devices based on the ABX_3 inorganic-organic hybrid perovskite $(CH_3NH_3)PbI_3$,[1,2, 3] hold the promise of cost effective solar energy production although reproducible device performance has not been achieved. Many questions remain to be addressed regarding the crystal chemistry of these materials, and the nature of charge transfer, before it will be possible to rationally modify and tailor chemistries and nanostructures in prototype solar cells for greater efficiencies. It is also notable that the rapid expansion of the device literature has overlooked important fundamental studies reaching back some 60 years. Therefore, it is timely to review the sometimes conflicting reports concerning $(CH_3NH_3)PbI_3$ and related materials, and exploit state-of-the-art methods to revise and evaluate their crystal structures and photo-conversion mechanisms.

2. Crystallographic and Functional Character of Hybrid Perovskites

The perovskite aristotype is a cubic *Pm*-3*m* framework structure of composition ABX_3, where *A* (Wyckoff position 1*a*) is commonly a large cation coordinated to 12 *X* (3*c*) anions, *B* (1*b*) a smaller metal bonded to six *X* anions, and BX_6 octahedra are corner-connected to form a three-dimensional framework. The hinged octahedra allow for wide adjustment of the *B*-*X*-*B* bond angle, and several sets of cooperative rotations, known as tilt transitions, promote symmetry reduction of the aristotype.[4-6] The process of octahedral tilting must adhere to the principles of space group hierarchy and these relationships provide a powerful tool for guiding structure determination and detecting false structures. In this respect, it is noted that some

structures for the $(CH_3NH_3)PbX_3$ polymorphs are inconsistent with space group principles. Furthermore, for organic-inorganic hybrid-perovskites the interaction of cation ordering and acoustic modes can generate incommensurate phases in many of these compounds.[7]

ABX_3 (A = alkali; B = Ge, Sn, Pb; X = halide): The unusual, and potentially useful, electronic and photoconductive properties of plumbohalide perovskites were identified several decades ago by Møller[8, 9] who determined the crystal structures of $CsPbX_3$ (X = Cl, Br, I) and found intense colours ranging from yellow, orange to black for the chloride, bromide and iodide analogues respectively. All the materials were photoconductive with spectral sensitivity maximised in the violet (X = Cl), blue-green (X = Br) and red (X = I).[9] X-ray diffraction revealed perovskite hettotypes at ambient that undergo a displacive phase-transition to cubic symmetry at higher temperature. $CsPbCl_3$ was optically birefringent at room temperature, but upon heating, the interference colours changed continuously and disappeared at 46.9°C. This phenomenon was completely reversible and on cooling the interference colours reappeared. Møller[8] reported that below the transition temperature the $CsPbCl_3$ was tetragonal, with chlorine displaced from the *Pm*-3*m* special position (½, 0, 0) to (½, ±1/15, ±1/15) and caesium ideally at (½, ½, ½) drawn out in directions perpendicular to the unit-cell faces. Significantly, this early work found 3D symmetry could not unambiguously describe the mean positions of chlorine, but only their 'statistical centres of gravity'; subsequently it was suggested a high level of anion disorder[10] and/or incommensuration[11, 12] was present.

The positioning of Pb^{2+} at the octahedral '*B*' site of ABX_3 perovskites is unusual, as in most perovskites lead is an *A*-site cation, but this placement becomes feasible when a large electropositive cation occupies the '*A*' site. Cs^+ most evidently meets this criteria, as do

similarly sized organic units including methylammonium (*MA*) $(CH_3NH_3)^+$, formamidinium $(H_2N\text{-}CH{=}NH_2)^+$ (FA) and tetramethylammonium $((CH_3)_4N)^+$ (*TMA*). The first 'hybrid' organic-inorganic perovskites, described almost 35 years ago,[13] were based on halide salts of the group 14 chalcogenides, with germanium, tin and lead occupying the octahedral *B*-sites, and *MA* and *TMA* radicals inserted in the cages formed by the BX_6 octahedra. For these perovskites, superlattices often result due to orientational ordering of the organic cations coupled with tilting and distortion of the octahedra. By introducing longer chain organic components, perovskite-type layer compounds comparable to the Ruddlesden-Popper series are created. These modifications have been comprehensively reviewed by Mitzi.[14, 15]

In group 14 elements the outer s^2 electron pair can become sterochemically active lone pairs, rather than participating in bonding, a tendency most evident at higher atomic number. Clark *et al.*[16] undertook an extensive study of the $CsM^{2+}X_3$ (M^{2+} = Ge, Sn, Pb; X = Cl, Br, I) compounds and found evidence for the band structure being populated by non-bonding electron pairs. The optical behaviour and electrical conductivity of these phases was presumed to arise from the donation of electron density from M^{2+} lone-pair electrons to the conduction band formed by overlap with the halogen *d* states. The greater ionic character of the Pb^{2+}, as compared to Sn^{2+}or Ge^{2+}, reduced the electron density transfer and dominated the optical spectra of the Pb-rich phases. For $CsM^{2+}I_3$ the donation of electron-pairs to iodine *d* bands was favoured over the self-population by iodine electrons.

A recent temperature-dependent powder synchrotron X-ray diffraction study[17] confirmed earlier reports[18] by showing that at room temperature $CsSnI_3$ is orthorhombic (*Pnma*) and with gentle heating converts to the *Pm*-3*m* aristotype via a *P*4/*mbm* tetragonal variety (Table 1). In this work,

the $CsSnI_3$ system appeared to be unique in combining two generally contraindicative properties, strong photoluminescence and high electrical conductivity. More recently the F doped phase $CsSnI_{2.95}F_{0.05}$ has achieved one of the highest conversion efficiencies (8.5%) found in solid-state dye-sensitised solar cells.[19]

ABX_3 (A = organic cation; B = Ge, Sn, Pb; X = halide): The effect of *s*-orbital hybridisation in *ABX_3* perovskites is to drive the *B*-atom off the octahedral centre, resulting in alternating long and short *B-X* bonds in the basal plane that creates a range of functionalities. In the widely studied Ge analogues, ferroelectric behaviour is found in $CsGeCl_3$,[20, 21] antiferroelectricity in *TMA*$GeCl_3$,[22] and high Cl-ion conductivity in *MA*$GeCl_3$.[23] For the cubic phases of *MA*$GeCl_3$,[23] *TMA*$GeCl_3$[24] and *TMA*$GeBr_3$[25] the disordered halide ions half-fill and statistically occupy the 6*f* Wyckoff site of *Pm*-3*m*, rather than a fully occupied 3*c* site, due to bond switching between Ge -X…Ge and Ge...X-Ge, i.e. distortion associated with lone-pair activity is a very soft-coupled dynamic reorientation with respect to the organic (*TMA* or *MA*) cation. In these cases, the GeX_6 the coordination is often described as pyramidal with 3 short and 3 long bonds rather than octahedral. In *MA*$GeCl_3$ ^{35}Cl nuclear quadrapole (NQR) measurements found reorientation of the pyramidal $GeCl_3^-$ is the origin of the high ionic conductivity.[23-26]

X-ray diffraction has been the primary source of crystallographic information for these perovskites, but scattering is dominated by higher atomic number elements, and is relatively insensitive to the organic component that controls phase transitions. This was addressed by Yamada *et al.*[26] who carried out a powder neutron diffraction study on deuterated *MA*$GeCl_3$ ≡ $CD_3ND_3GeCl_3$, but substitution of H for D strongly shifted the polymorphic phase transition temperatures with four distinct structures in the temperature range 2 – 475K (Table 2).

The crystallochemical properties of Sn-based analogues are intermediate to Ge and Pb compounds, such that the inorganic sublattice of *MA*$SnBr_3$ in the *Pm*-3*m* phase has stronger and more complex octahedral distortions than the Pb-based analogues. A powder X-ray diffraction study of *MA*$SnCl_3$ showed successive transitions to high symmetry phases at 283, 307, 331 and 463 K with increasing temperature (Table 3);[27] the high temperature (463 K) phase was cubic perovskite with lower temperature distortions containing a pyramidal $SnCl_3^-$ ion. Modification of Sn-coordination was established with ^{119}Sn NMR spectra and suggested the onset of chloride-ion diffusion just below the phase-transition to cubic symmetry.

A powder neutron diffraction study of deuterated *MA*$SnBr_3$ ≡ $CD_3ND_3SnBr_3$ found a cubic polymorph (*Pm*-3*m*, Z = 1, a = 5.899 Å) at room temperature, that at 195K transformed to a rhombohedral superstructure with cell doubling in three directions (*R*3*c* or *R*-3*c*, Z = 8, a = 11.767 Å α = 88.997°).[28] A subsequent synchrotron XRD study found no evidence of the rhombohedral phase on cooling from 230 – 100K, but did identify an orthorhombic phase in the temperature range 230 – 188K ($Pmc2_1$, Z = 2, a = 5.89406(17) Å, b = 8.3862(2) Å, c = 8.2406(2) Å).[29] At 30K the presence of a triclinic phase was suggested, and indexing of Bragg reflections gave the best candidate cell as a = 8.345 Å b = 8.135 Å c = 5.899 Å α = 92.14° β = 89.95° γ = 91.42° in *P*1 symmetry. The lack of an inversion centre (*P*-1) was assumed due to its absence in the orthorhombic cell, but as noted in this study, it is impossible to directly transform *Pm*-3*m* to $Pmc2_1$ from pure octahedral tilts, and an intermediary phase was not identified. A tetragonal *P*4/*mbm* phase was suggested as the most likely candidate, by analogy with the non-cubic phase encountered on cooling the alkali analogue $CsSnBr_3$.[30]

A single crystal neutron diffraction study of the high temperature *Pm*-3*m* phase of *MA*$PbBr_3$ revealed a highly disordered structure. This work suggested positions for the C/N and H sites of the methylammonium groups but it was noted that there was a large anisotropy in all the atomic displacement parameters.[31] A powder neutron diffraction study of partially deuterated *MA*$PbBr_3 \equiv CH_3ND_3PbBr_3$ found the 'phase IV' of this series was centrosymmetric, *Pnma*: $Z = 4$, $a = 7.9434(4)$ Å, $b = 11.8499(5)$ Å, $c = 8.5918(4)$ Å at 11 K,[32] leading to speculation that the corresponding iodide would be isostructural. In the original work of Poglitsch and Weber four different phases were identified for the lead bromide series and space groups suggested from the X-ray extinction conditions at various temperatures ($T > 236.9$ cubic *Pm*-3*m*; $155.1 < T < 236.9$ tetragonal *I*4/*mcm*; $149.5 < T < 155.1$ tetragonal *P*4/*mmm*; $T < 144.5$ orthorhombic $Pna2_1$).[33] The space group *P*4/*mmm* was erroneously suggested for a second tetragonal intermediary phase as this cannot be achieved by octahedral tilting from the *Pm*-3*m* aristotype.[6] High pressure structural studies on *MA*$PbBr_3$ showed that just below 1GPa the sample transformed from *Pm*-3*m* to *Im*-3 and amorphised at 2.8GPa without the cations undergoing long-range orientational ordering.[34] The *Im*-3 cell has a doubled cell parameter with respect to the un-tilted *Pm*-3*m* phase and the sample recrystallised upon the release of pressure. In general, phase transitions through cooling or applied pressure often track but for hybrid organic-inorganic perovskites the *Pm*-3*m* → *Im*-3 transition under compression is presently unique. This implies the energy gain for orientational ordering was low and volume reduction is the driving force for transitions of these compounds under pressure.

The synthesis of the *MA*PbI_3 was first described by Weber[13] who reported the cubic perovskite (*Pm*-3*m*, $Z = 1$) at high temperature. Since the cubic structure only contains one formula unit per

unit cell, the noncentrosymmetric methylammonium ions $(CH_3NH_3)^+$ with C_{3v} symmetry must be orientationally disordered to satisfy O_h symmetry, such that the radial cation is statistically distributed over eight identical (x, x, x) positions, in which the C and N atoms show random distribution inside the eight tetrahedral interstices of the *A*-site cubooctahedra of the perovskite aristotype i.e. 24 disordered states. Rapid reorientation motions of $(CH_3NH_3)^+$ were detected by variable temperature NMR that revealed two phase transitions as the temperature decreases, as a result of progressive ordering of the $(CH_3NH_3)^+$ ions.[35] The first phase change to tetragonal *I*4/*mcm* (T_c = 327.4K), lowered the number of disordered states of the $(CH_3NH_3)^+$ to 8, while in a lower temperature $Pmc2_1$ orthorhombic phase (T_c = 162.2K) the organic cations are fixed. Kawamura *et al*.[36] studied the tetragonal to cubic transition by means of single crystal X-ray diffraction and found with decreasing temperature the rotation angle of the octahedron increased monotonically, suggesting that this is an order parameter of the cubic-tetragonal transition. The cubic structures of the $MAPbX_3$ (X = Cl, Br, I) were also studied by single crystal X-ray diffraction, which revealed heavily disordered structures with high atomic displacement parameters, particularly those of the anions.[10]

The phase transitions in $MAPbI_3$ have also been studied using calorimetric and infrared spectroscopy.[37] This work found an orthorhombic → tetragonal transition at 161.4K, with the tetragonal → cubic transition at 330.4K. While both phase transitions were first-order, the higher temperature phase change was close to second-order. The observed entropies were consistent with order-disorder transitions interpreted with three models where the methylammonium ions disorder with respect to the orientation of the C-N axis itself and around the C-N axis. It was found that the infrared line width of particular vibrations of the

methylammonium ion changed markedly with temperature due to hindered rotational motion in the cubic and tetragonal phases.[37]

The dielectric properties of *MA*PbI_3 [33, 38] show a discontinuity of the real part of the dielectric permittivity at the orthorhombic → tetragonal phase transition, but with the tetragonal → cubic transition. These observations would be consistent with the methylammonium ions being fully disordered in the cubic and tetragonal phases, and completely ordered in the orthorhombic phase.

Herein, we report the synthesis of *MA*PbI_3 in both poly- and single crystalline form that have been crystallographically characterised using variable temperature single crystal X-ray diffraction, variable temperature powder X-ray diffraction and phase contrast transmission electron microscope imaging. The higher temperature polymorphic transitions were monitored using thermogravimetic analysis and differential scanning calorimetry. The optical band gap for *MA*PbI_3 determined by UV-Visible spectroscopy was compared to values obtained from density-of-state simulation of the electronic band structure.

3. Experimental

3.1 Synthesis

Method 1 – Polycrystalline *MA*PbI_3 was prepared by precipitation from a hydroiodic acid solution. Following Poglitsch *et. al.*[33] 2.5g of lead(II) acetate (Chemical Reagents, Sigma) was dissolved in 10 ml of a concentrated (57% by weight) aqueous HI contained in a pyrex test tube and heated in a water bath. An additional 2 ml of HI solution with 0.597g of CH_3NH_2 (40%

soluble in water, Merck) was added to the solution. A black precipitate that formed upon cooling from 100 ºC to 46 ºC over 6 hours was then filtered and dried (100 ºC/10 hours). It proved essential to maintain the solution above 40°C as lower temperatures favour the incorporation of water of crystallisation and the formation of yellow crystals of $MA_4PbI_6{\cdot}2H_2O$.[39] Large $MAPbI_3$ crystals were grown as described but with a very much slower cooling rate. Black crystals up to 2mm long were obtained by cooling the solution over 4 days. Crystallisation proceeded most rapidly at approximately 70°C.

Method 2 – $MAPbI_3$ was synthesised using the method described by Im *et. al.*[1] from an equimolar mixture of *MA*I and PbI_2 in gamma-butyrolactone. To begin, *MA*I was synthesised by reacting a concentrated aqueous solution of hydroiodic acid (Sigma Aldrich) with methylamine (40% in methanol) at 0°C for 2h with constant stirring. After evaporation at 50°C in a rotary evaporator the resulting precipitant was washed three times with ethyl ether and dried in vacuum at 60°C for 24h. Equimolar mixtures of the as-synthesised *MA*I and PbI_2 (99%, Sigma Aldrich) in gamma-butyrolactone (Sigma Aldrich) were left to stir overnight at 60°C. The $MAPbI_3$ product was obtained by drop-casting the as-prepared solutions on to glass substrates, which were then heated to 100°C and annealed for 30min. Crystalline $MAPbI_3$ was recovered from the glass after cooling.

3.2 Crystallographic Characterisation

Powder X-ray diffraction: Phase purity was confirmed by powder X-ray diffraction (PXRD) patterns collected with a Bruker D8 Advance diffractometer (Bragg-Brentano geometry)

equipped with a Cu *Kα* X-ray tube operated at 40 kV and 40 mA using a step size of 0.02° and a time per step of 4s. Samples were mounted in a top-loaded trough, which was rotated during data collection. Under these conditions, the intensity of the strongest reflection was approximately 10000 counts. Experimental fitting of the X-ray data was carried out from 10-140° 2θ using *TOPAS V4.1*[40] and employing the fundamental parameters approach[41] and a full axial divergence model.[42]

The tetragonal → cubic phase transition was investigated using variable temperature powder X-ray diffraction. In-situ XRD data were collected in asymmetric reflection mode under a static helium atmosphere on an INEL Equinox 3000 (Inel, Artenay, France) equipped with an XRK-900 reactor chamber (Anton-Paar, Graz, Austria), a curved position sensitive detector (Inel, Artenay, France), a copper *Kα* source and a Ge-(111) focussing mirror. The material was mounted on a closed steel sample holder and measured with a fixed incident beam angle of 5°. Two different heating experiments were conducted. In the first, the *MA*PbI_3 was heated to 85°C in five degree steps starting from 25°C, with data collected for 5 minutes at each holding temperature. The second experiment employed a continuous heating ramp at a rate of 1°/min during which 30 measurements of 120 seconds were performed. Each measurement corresponds to a temperature span of 2°C; the final temperature of each measurement was recorded in the measurement file. Five empty sample holder measurements were conducted at room temperature in order to establish the chamber background. First, the data were truncated to an angular range of 4 to 60° in 2θ. Then the average of the 5 background measurements were subtracted from each pattern in order to get the pure diffraction patterns without any chamber contributions. Finally, all individual diffraction patterns of each experiment were collated into a single *xty* - file

(x = 2θ, t = temperature, y = intensity). DPlot[43] was used to generate the figures displaying the results from these experiments. The variation in lattice parameters with temperature was extracted from a Pawley fit of the diffraction patterns and assuming a tetragonal cell with lattice parameters close to those previous reported. The zero-error shift was refined in the data collected at 25°C and fixed at that same value for all subsequent temperatures. The sample displacement was refined in all data sets with T > 25°C but constrained to take a value less than that obtained in the previous temperature measurement. This constraint was used because a prior measurement with an Al_2O_3 standard showed the thermal expansion of the sample holder leads to increasingly lower values of sample displacement.

Single crystal X-ray diffraction: A small fragment (approximately 0.1 mm × 0.1 mm × 0.1 mm) was cleaved from one of the solution grown single crystals. Data were collected on a Bruker Smart Apex II three-circle diffractometer at various temperatures between room temperature and 100 K using Mo *K*α radiation with a graphite monochromator over the angular range 2.5 to 30.5° 2θ. The Saint module, deployed within Apex II, was used for reflection integration and performing Lorentz polarisation and multiscan absorption corrections. A total of 17319 reflections with $I>3\sigma(I)$ were collected and the structures refined using Jana 2006 [44] utilising the Superflip [45] structure-solution algorithm. Three dimensional difference Fourier maps were visualised using the software VESTA.[46]

Transmission Electron Microscopy: Powdered samples deposited on holey carbon copper grids were analysed using transmission electron microscopy (TEM) with a JEOL JEM 2100F instrument equipped with a double-tilt holder. Field limiting apertures for selected area electron

diffraction (SAED) were 5, 20 and 60 μm in diameter. High-resolution images were collected using a high-contrast objective aperture of 20 μm, corresponding to a nominal point-to-point resolution of 0.17 nm. Simulation of kinetic and multi-beam electron diffraction patterns as a function of crystal thickness and beam divergence was performed using JEMS.[47] Electron energy loss spectroscopy (EELS) was carried out by using the JEOL JEM 2100F microscope operating at 200 kV. EELS spectra were recorded with an energy dispersion of 0.25 eV/ch, and the background was subtracted by fitting a region before the ionisation edge with the power-law model followed by extrapolation and removal of the background from under the edge.

3.3 Thermal Analysis

Thermogravimetric (TGA) analysis of was performed on a TGA Q500 V6.7 (TA Instruments) in an interval from 34°C to 500°C at a ramp rate of 5°C/min under Ar gas and in air with a flow rate of 40ml/min. Differential scanning calorimetry (DSC) was conducted on a Q10 V9.9 Build 303 calorimeter (TA Instruments) at a rate of 5°C/min over a temperature range from 25°C to 200°C under Nitrogen. Approximately 10mg of *MA*PbI_3 was used in each experiment.

3.4 Diffuse UV-Visible Spectroscopy

The optical diffuse reflectance spectra of *MA*PbI_3 perovskite powder were measured at room temperature using a UV-VIS-NIR spectrophotometer (Shimadzu UV-3600) with integrating sphere attachment (ISR-3100) operating in the 300-1500 nm region. Highly refined barium sulfate powder (Wako, pure) was used as a reflectance standard.

3.5 Electronic Structure Calculations

Lattice constants and atomic coordinates derived from the present study were used to calculate the electronic band structures and the densities of the states (DOS) for the polymorphs without further optimisation. The calculations were based on density functional theory[48] (DFT) where the generalised gradient approximation (GGA) of Perdew-Burke-Ernzerhof (PBE)[49] was used to represent the exchange and correlation energy of the electrons with the CASTEP[50] code. The Brillouin zone summation was performed by using 4 × 4 × 4 *k*-point grids for sampling in the Brillouin zone. In the cubic (*Pm*-3*m*) and tetragonal (*I*4/*mcm*) phases, the $CH_3NH_3^+$ cation is dynamically disordered.[27] Takahashi[51] performed the band structure calculation using fixed $CH_3NH_3^+$ for the same class of semiconducting perovskite halides *MA*SnI_3, however this reduced the symmetry and made it difficult to determine accurate band structures.[52] Based on the previous studies,[53-55] the electronic properties are strongly dependent on the inorganic components, i.e. the $[PbI_6]^{-4}$ networks. Therefore $CH_3NH_3^+$ was ignored in our calculations and a uniform background charge density was added to neutralise the charge, except for the orthorhombic (*Pnma*) phase, from which the atomic positions of $CH_3NH_3^+$ were determined by single crystal XRD.

4. Results and Discussion

The methods used to synthesise *MA*PbI_3 were successful in preparing high quality samples in both poly- and single crystalline form (Figure 1). All samples were black, but slowly became

yellow, when exposed to a humid atmosphere, with conversion to the hydrated phase $MA_4PbI_6{\cdot}2H_2O$ ($P2_1/n$ a = 10.421(3) Å, b = 11.334(2) Å, c = 10.668(2) Å, β = 91.73(2)°, Z = 2). The single crystals of $MAPbI_3$ generally formed as dodecahedra, with some examples exhibiting faceting consistent with rhombo-hexagonal dodecahedra, which is a typical crystal habit of a body centred tetragonal lattice, in agreement with the reported structure at room temperature (space group $I4/mcm$). Using the lattice parameters and space group for the tetragonal structure*[i] reported by Kawamura *et al.*[36] a Pawley fit of the powder X-ray diffraction pattern showed the desired phase had been successfully synthesised (Figure 2).

At higher temperatures (≈327 – 330K; ≈54 – 57°C) the tetragonal perovskite reportedly becomes cubic. To investigate this transition in more detail we carried out variable temperature powder X-ray diffraction on an Inel Equinox diffractometer that has a large detector and collects intensity data over the entire 2θ range simultaneously, and so is ideal for monitoring phase transitions or in-situ reactions. Comparison of the calculated powder X-ray diffraction patterns for $MAPbI_3$ in cubic (Pm-3m) and tetragonal ($I4/mcm$) symmetry (Figure 3), show that these polymorphs are readily differentiated by monitoring the intensities of the {211} and {213} reflections as they are sufficiently separated from Bragg reflections expected in cubic symmetry. The {211} reflection has a higher calculated intensity so any change in symmetry would be detected more easily by monitoring this reflection. The variable temperature XRD patterns collected at 2°C intervals between 25 – 85°C show that close to 57°C there is a clear reduction in {211} positioned at 23.5° 2θ, which gradually disappears towards higher temperature (Figures 4 and 5). Although there is a large change in diffraction intensity at 57°C weak scattering persists

[i] * Note the fractional coordinate of I(1) as reported is incorrect. The values should be x = 0.2039(8), y = -0.2961 (negative of published value) z = 0

to 75°C. This change in intensity is an agreement with previously reported transition temperatures and also with the DSC plot where heating and cooling curves, yield maxima at 57.3°C and 56.0°C respectively (Figures 6 and 7). The DSC peaks are asymmetric (Figure 6), which may be indicative of a transient intermediate phase undetected by powder X-ray diffraction. One possibility could be a *Pm*-3*m* to *Im*-3 transition analogous to that found in the high pressure study of *MA*$PbBr_3$,[34] however further work is needed to verify this. The origin of differences in the transition temperatures shown in the heating and cooling plots are unclear but may arise from minor absorbed H_2O incorporated at room temperature (Figure 7). This is supported by a feature in the DSC plot close to 100°C in the heating curve, which is absent in the cooling curve. There is an inflection in the cooling curve at approximately 75°C, absent in the heating curve, that corresponds to the initial appearance of the {211} reflection in the variable temperature powder XRD study. The presence of absorbed H_2O is also agreement with a TGA experiment carried out in air which showed a small mass loss at $T > 80$°C (c.a. 0.3% of the original mass). Previous TGA experiments carried out in air showed that the perovskite phase is stable up to ≈ 280°C, after which there is an abrupt and significant mass loss of 47.3% suggestive of complete decomposition.[1] The volatilisation $(CH_3NH_3)I$ + ½ I_2 would be an approximate 46.1% weight loss, however as the TGA is conducted in air this is likely to proceed with the co-formation of an lead-oxide-iodide such as Pb_2OI_2. The decomposition of PbI_2 in air is complex and the TGA study of Krämer and Post[56] identified several lead-oxide-iodide phases during conversion of PbI_2 to PbO. For comparison, a TGA experiment under argon gas using perovskite that had been stored in a dry-box and therefore free from absorbed water found the sample to be stable up to ≈ 300°C, and the 66.6% weight loss at 360°C is consistent with the complete decomposition to Pb metal (Figure 8). The refined lattice parameters as a function of

temperature show much more variation in the crystallographic *c* axis as the temperature approaches the transition temperature and discontinuity in cell volume (Figure 9 and Table 4).

Single crystal X-ray diffraction at room temperature gave the expected tetragonal cell but with reflection conditions consistent with the space group *I*4/*m* and not the reported *I*4/*mcm* symmetry. However, *I*4/*m* symmetry is not compatible with perovskite space group hierarchy,[6] and refinement was unsuccessful; the anomaly may be a consequence of extensive disorder from PbI_6 tilting or antiphase boundaries. Treating the data in the expected *I*4/*mcm* symmetry allowed the location of Pb and I, but as in previous work, the disordered $(CH_3NH_3)^+$ units cannot be modelled unambiguously.[32, 36] Notably in the single crystal study of the tetragonal phase carried out by Kawamura *et al*.[36] only used reflections where $F_o > 5\sigma F_o$ rather than the conventional 3σ precision.

MAPbI_3 undergoes a tetragonal to orthorhombic phase transition at approximately 161K (≈ -112°C).[33, 38] Poglitsch and Weber used Guinier-Simon photographs to determine the orthorhombic polymorphs of both the bromide and iodide in the non-centrosymmetric space group $Pna2_1$.[33] However, Swainson *et al*.[32] reclassified the bromide in the centrosymmetric space group *Pnma*, as refinements and subsequent symmetry analyses in $Pna2_1$ was suggestive of missing symmetry elements. This latter work also speculated the iodide analogue would adopt the same symmetry. In addition, although the polar space group $Pna2_1$ was originally assigned to the bromide and iodide, no ferroelectric properties have been reported so far.[57] Swainson *et al.*[32] highlighted that in the original work of Poglitsch and Weber,[33] no structural information was given and only the Guinier film was used to suggest $Pna2_1$.

In this study, single crystal X-ray diffraction at 100K yielded an orthorhombic, *Pnma* cell and a structure solution using the Superflip algorithm,[45] readily located the Pb and I positions, with the C and N sites identified from the difference Fourier maps. The refinement proceeded smoothly to yield the refinement residuals, atomic coordinates and atomic displacement parameters listed in Tables 6 and 7. Refinements were also performed in the space group $Pna2_1$; however these offered no real improvement in the refinement residuals and gave no indication for the absence of an inversion centre. One feature that was present in refinements in both space groups were some relatively strong regions of positive and negative electron density at distances unreasonably close to the iodine positions (Figure 10). The I(1) apical position had disc shaped atomic displacement ellipsoids with regions of negative and positive electron density close to the refined positions (<1 Å). The I(2) equatorial site also has a strong region of positive electron density in close location to their sites. Similar features in the difference Fourier maps were noted by Mashiyama *et al.*[10] in the high temperature single crystal X-ray diffraction study of the cubic forms of $MA\mathrm{Pb}X_3$ (X = Cl, Br, I). One explanation for these features could be that the motion of the anion positions are better described using an anharmonic displacement model as successfully applied to the cubic systems of $\mathrm{CsPb}X_3$ (X = Cl and Br).[58] Single crystal neutron diffraction experiments are now planned to investigate the latter possibility in more detail. Alternative attempts have been made to quantify the disorder observed in a range of organic-inorganic perovskites using X-ray pair distribution functions.[59] This work found the local structures of such materials showed angular distortions of the octahedra, such that the halides have a significant displacement transverse the midpoint of the *B-B* distance to which they are

constrained in the ideal crystallographic description. These displacements are likely dynamic in nature, due in part to the presence of soft transverse acoustic phonons in these structures.

As noted in the work by Swainson *et al.*[32] in their structural analysis of *MA*$PbBr_3$, there is no group-subgroup relationship between *I*4/*mcm* and *Pnma*, so it is impossible to descend continuously through this sequence. It is therefore likely that a transient intermediary phase for both the bromide and iodide analogues exists, but this has yet to be experimentally observed. Poglitsch and Weber suggested a second tetragonal phase for the bromide with *P*4/*mmm* symmetry;[33] however this is not one of the space groups that can be generated from pure tilt transitions.[6] To further investigate this we monitored the variation in lattice parameters as a function of temperature using single crystal X-ray diffraction (Figure 11 and Table 8). The absolute temperatures shown in this study should be treated with caution as the temperature recorded is the temperature at the sensor positioned on the nitrogen nozzle rather than the crystal itself. Nevertheless, we observed a clear discontinuity and a change in lattice parameters consistent with the reported orthorhombic to tetragonal phase transition close to 161K.[33, 38] We investigated the suggested space groups from indexing the diffraction data close to transition region. The data collected at 152K suggested the space group *Ibam*, however this space group is inconsistent with reported perovskite symmetries and further experiments will be required to explain this feature.

Transmission electron microscopy revealed that the perovskite is remarkably stable under the 200 KeV electron beam. Samples containing heavy elements such as Pb and I are often found to decompose during electron beam irradiation because of the energy deposited during electron

beam absorption. It is suggested that the presence of the methylammonium ion that contains relatively lighter elements help dissipate the electron energy. High-resolution TEM images revealed a well ordered crystal, but the diffracted intensities of the selected are electron diffraction patterns and fast Fourier transform reconstructions were inconsistent with both the room temperature *I*4/*mcm* and high temperature *Pm*-3*m* phases as determined by powder X-ray diffraction. Extensive pattern simulation as a function of crystal thickness and beam convergence were unable to replicate the observed patterns (Figure 12). Other symmetries such as *Pn*-3*m* offered slightly better but not fully convincing matches. It seems probable that *Pm*-3*m* represents an average structure that satisfactorily accounts for intensity in the X-ray diffraction patterns. However at the micron scale, local symmetry and/or occupancy vary and some SAD patterns suggest higher dimensional order. The electron-energy loss spectrum (EELS) shows clear *K*-edge for I atoms, while N *K*-edge is very weak (Figure 13). The background-subtracted EELS spectrum shows a clear N edge onset at 403eV thus confirming the presence of the $(CH_3NH_3)^+$ units (insert Figure 13).

Diffuse reflectance UV-Vis spectra were used to calculate the optical absorption coefficient (α) according to the Kubelka-Munk equation,[60] $F(R) = \alpha = (1-R)^2/(2R)$, where R is the reflectance (%) (Figure 14). E_g for the *MA*PbI_3 powder is determined to be 1.51 eV from the extrapolation of linear part of transformed Kubelka-Munk spectrum and the calculated band-gap is in good agreement with Kim *et al*.[2]

The experimentally observed band gap was compared with electronic band structure calculations derived from CASTEP,[50] including speculative calculations for the band-gaps of the cubic and

orthorhombic polymorphs of *MA*PbI_3. The electronic band structure along the high-symmetry *k* lines[ii] and the projected density of states show the cubic phase has a well-defined direct band gap of 1.3 eV at the *R* $(\frac{1}{2},\frac{1}{2},\frac{1}{2})$ point (Figure 15 (a)). The cubic structure transforms into tetragonal (*I4/mcm*) phase with the tilting of the PbI_6 octahedron around *c* axis, when temperature decreases, which moves the band to the Γ (0,0,0) due to the lowering of the lattice symmetry from *P* to *I* (Figure 15 (b)), and the band gap energy increases to 1.43 eV. This agrees with Borriello[55] and Chabot[52] who found the band gap becomes larger when the symmetry decreases and the tilting of octahedral network increases. The calculated band gap energy of tetragonal phase is slightly smaller than the experimental band gap 1.51 eV due to the underestimation with the DFT using GGA calculation. The projected density of states (PDOS) of cubic and tetragonal phases shows similarities (Figure 16 (a) and (b)). Both of the top valence bands mainly consist of *p*-orbitals of I with an overlapping of Pb 6*p* and 6*s* orbitals, while the bottom of the conduction band formed by the Pb 6*p*-I 5*s* σ-antibonding and Pb 6*p*-I 5*p* π-antibonding.[61] These similarities lead Umebayashi[61] to get a much smaller calculated band gap value (cubic data) than the experimental one (tetragonal data) without noting the phase difference.

As the dynamical disorder of methylammonium (MA) is removed in the orthorhombic (*Pnma*) phase, $CH_3NH_3^+$ can be considered in the calculation to show a direct band gap

---

[ii] The dispersion curves for the different Bravais lattices are shown along the following directions:

(a) Cubic: $\Gamma(0,0,0) \rightarrow X(0,\frac{1}{2},0) \rightarrow M(\frac{1}{2},\frac{1}{2},0) \rightarrow R(\frac{1}{2},\frac{1}{2},\frac{1}{2}) \rightarrow \Gamma(0,0,0)$;

(b) Tetragonal: $\Gamma(0,0,0) \rightarrow X(0,\frac{1}{2},0) \rightarrow M(\frac{1}{2},\frac{1}{2},0) \rightarrow R(\frac{1}{2},\frac{1}{2},0) \rightarrow Z(0,0,\frac{1}{2}) \rightarrow \Gamma(0,0,0)$;

(c) Orthorhombic: $\Gamma(0,0,0) \rightarrow Z(0,0,\frac{1}{2}) \rightarrow T(-\frac{1}{2},0,\frac{1}{2}) \rightarrow Y(-\frac{1}{2},0,0) \rightarrow S(-\frac{1}{2},\frac{1}{2},0) \rightarrow X(0,\frac{1}{2},0) \rightarrow U(0,\frac{1}{2},\frac{1}{2}) \rightarrow R(-\frac{1}{2},\frac{1}{2},\frac{1}{2})$

(E_g = 1. 61 eV) at the Γ (0,0,0) (Figure 15 (c)). The band gap energy increases after the transition to lower symmetry with further PbI_6 octahedral tilting along the *c* axis (Figure. 15). To evaluate the calculation in the cubic and tetragonal phases without inclusion of the *MA* cation radical, the same method was used for the orthorhombic structure with and without *MA* cation (Figure 17). The differences between the two different calculations are small, with a slightly lower band gap energy (1.57 eV) when *MA* is absent, perhaps due to smaller octahedral deformation. The PDOS (Figure 16(c)) of the orthorhombic phase shows that the bands due to the *MA* cation are situated in the middle of the valence band and lower energy region, and does not affect the band gap region. Elsewhere *ab initio* investigations of the low temperature triclinic phase of *MA*SnI_3 found the organic cation only contributes to bands that are far from the band-gap.[55] In summary, computation finds the organic part contributed exclusively to the electronic properties of hybrid organic-inorganic perovskites, but the band-gap energy is dominated by the inorganic component of these perovskite structures.

5. Conclusions

In this work, the perovskite *MA*PbI3 was successfully synthesised in both poly- and single crystalline form. Powder X-ray diffraction and DSC have confirmed the cubic to tetragonal phase transition at approximately 57°C, and TGA has shown that the material is stable up to around 300°C in an argon atmosphere. The low temperature orthorhombic structure has been solved for the first time in the space group *Pnma* and unusual features in the Fourier maps are suggestive of anharmonic displacements of the anions that require further investigation. Similarly, the mismatch in the calculated and observed intensities in the selected area electron

diffraction patterns are suggestive of localised symmetry differences in the room temperature tetragonal *I4/mcm* phase. Analysis of the known perovskite space group symmetries has revealed that there must be a transient phase between the tetragonal *I*4/*mcm* and orthorhombic *Pnma* analogues but the apparent *Ibam* symmetry close the transition temperature is inconsistent with the space group hierarchy, as is the observed *I*4/*m* for the tetragonal phase. It is evident that a combination of temperature dependant neuron diffraction, synchrotron X-ray diffraction and magic-angle spinning nuclear magnetic resonance (MASNMR) experiments are required to resolve the anomalies found in the literature and the present investigation. UV-Visible spectroscopy has revealed a band-gap of 1.51eV that is in good agreement with values obtained from DFT calculations and additionally show the band-gap will get larger as the symmetry is lowered. Furthermore, the band gap is relatively insensitive to the organic component of the structure. Although we have gathered structural information from the *MA*PbI_3 perovskite using a range of different techniques, inconsistencies in symmetry, and the likely disorder present in this and related materials must be understood to properly design and optimise devices.

6. Acknowledgements

Funding from the National Research Foundation (NRF), Singapore is gratefully acknowledged (CPR Award No. NRF-CRP4-2008-03). MG acknowledges support of this work by the Swiss National Science Foundation and the European Research Council under the Advanced Research Grant MESOLIGHT.

Figures and Tables

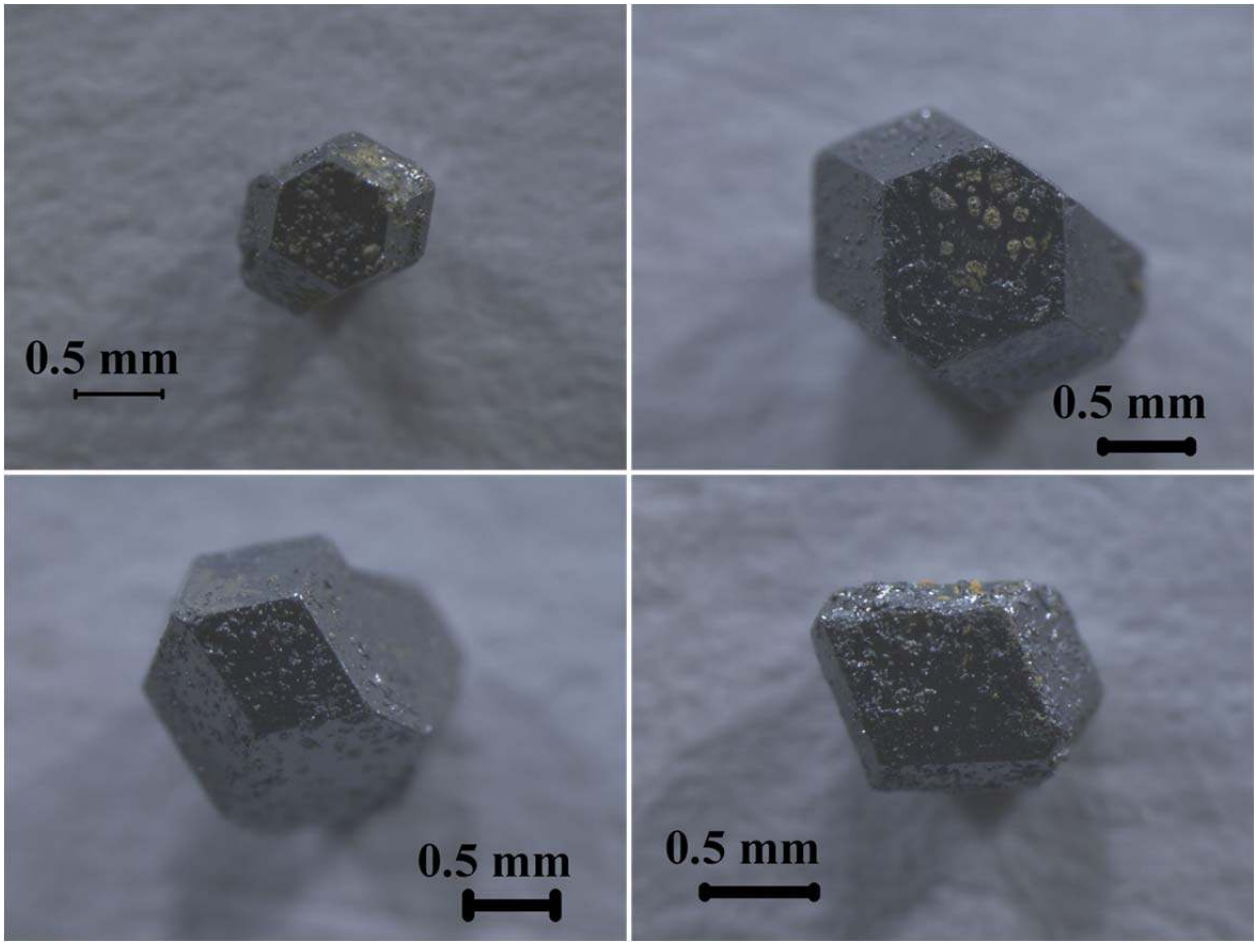

Figure 1. Example images of the single crystals grown using the method described by Poglitsch *et. al.*[33]

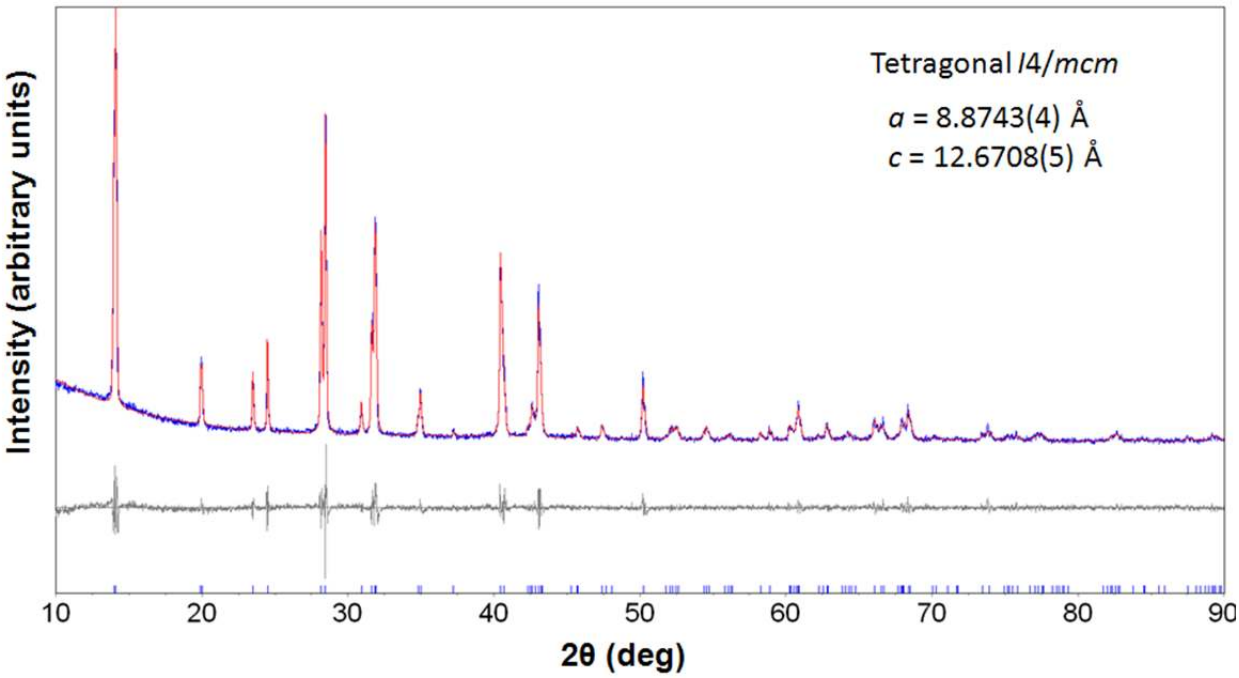

Figure 2. Pawley fit of the powder X-ray diffraction pattern of *MA*PbI_3 confirming a single-phase sample with tetragonal symmetry at room temperature.

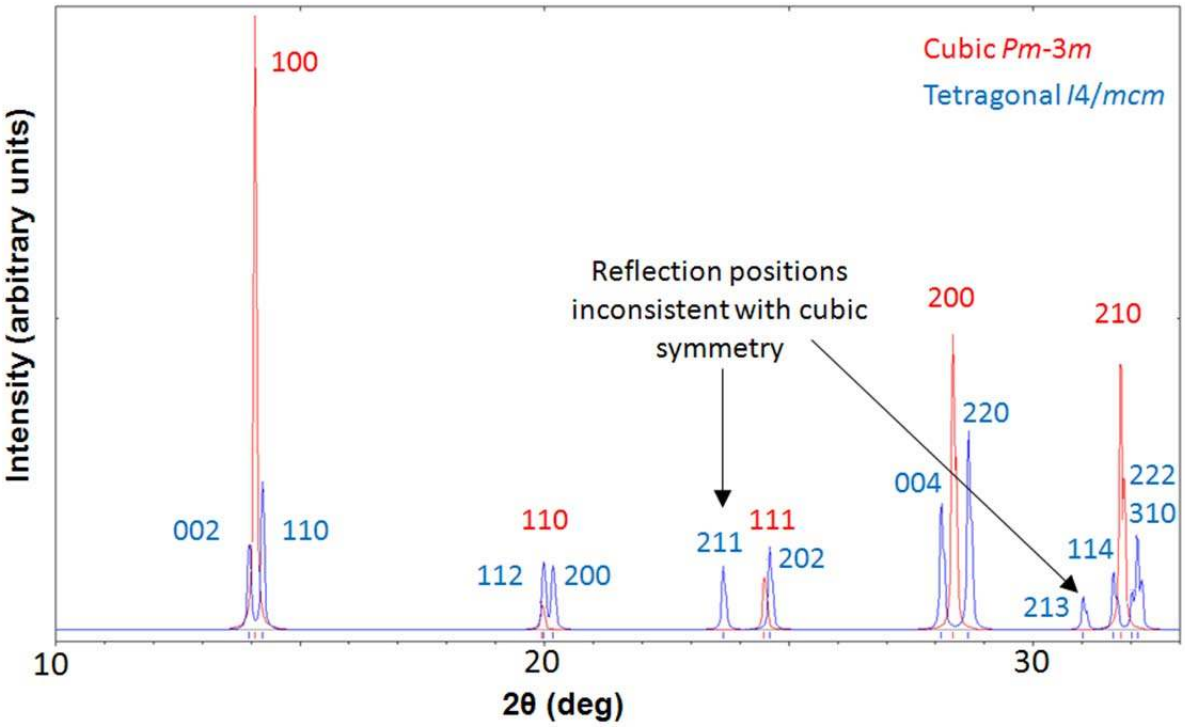

Figure 3. Calculated powder X-ray diffraction reflection positions for *MA*PbI_3 in both cubic and tetragonal symmetry respectively.

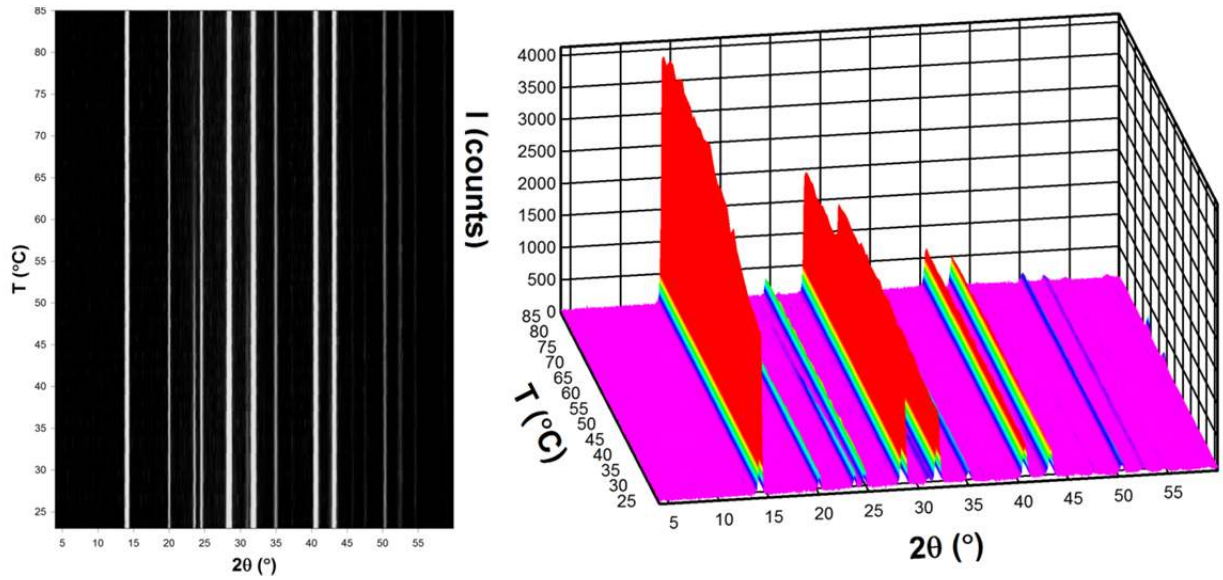

Figure 4. Two and three dimensional plots of the variable temperature powder X-ray diffraction patterns for *MA*PbI_3. Both plots show the gradual disappearance of the tetragonal super-lattice reflections.

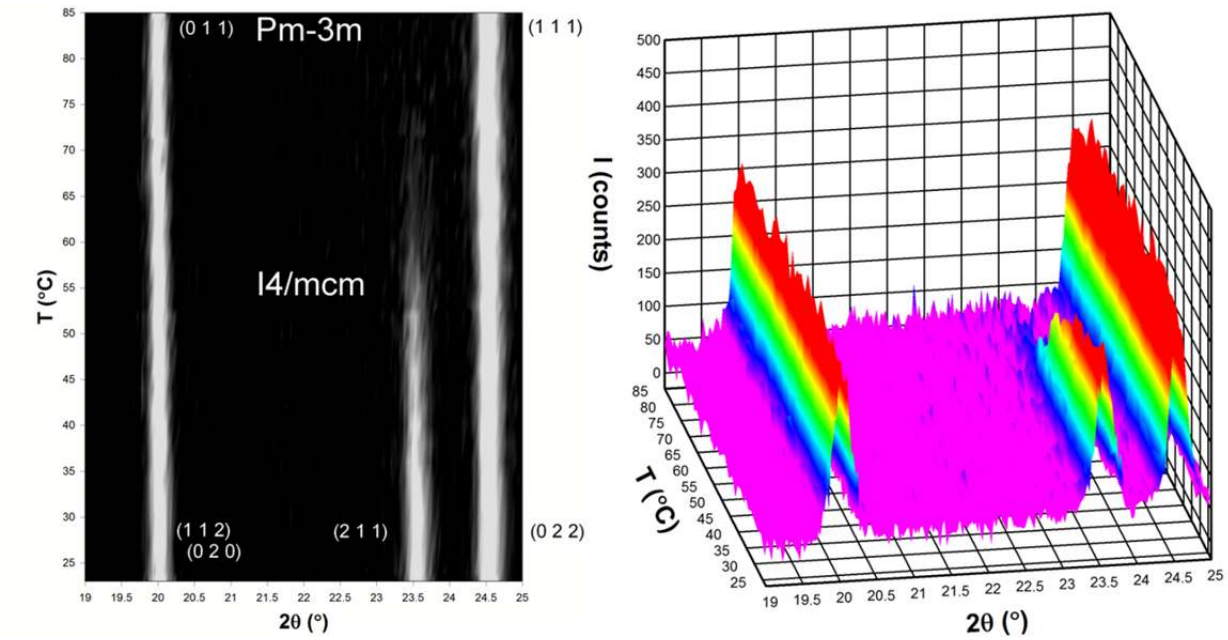

Figure 5. Expanded areas of the two and three dimension powder X-ray diffraction patterns, which show the gradual disappearance of the 211 reflection associated with the tetragonal supercell.

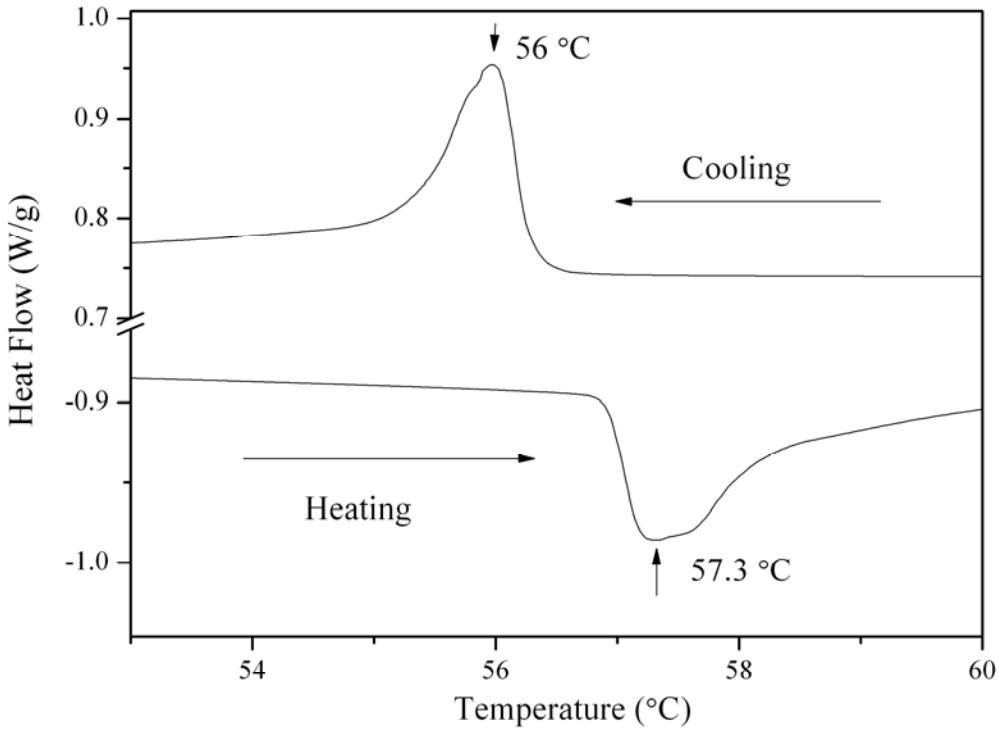

Figure 6. Differential scanning calorimetry (DSC) plot of the tetragonal → cubic transition.

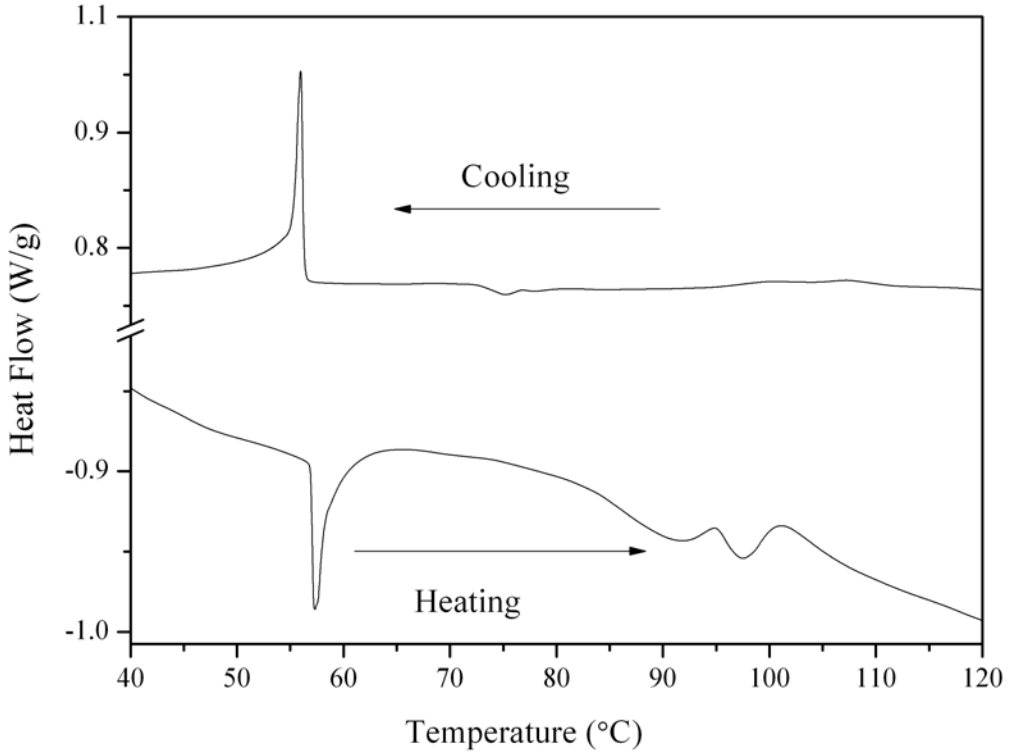

Figure 7. DSC plot for *MA*PbI_3 showing the tetragonal to cubic transition and a feature close to 100°C in the heating curve, which is absent in the cooling curve. It is suggested the latter feature indicates a small amount of absorbed H_2O was present in the sample.

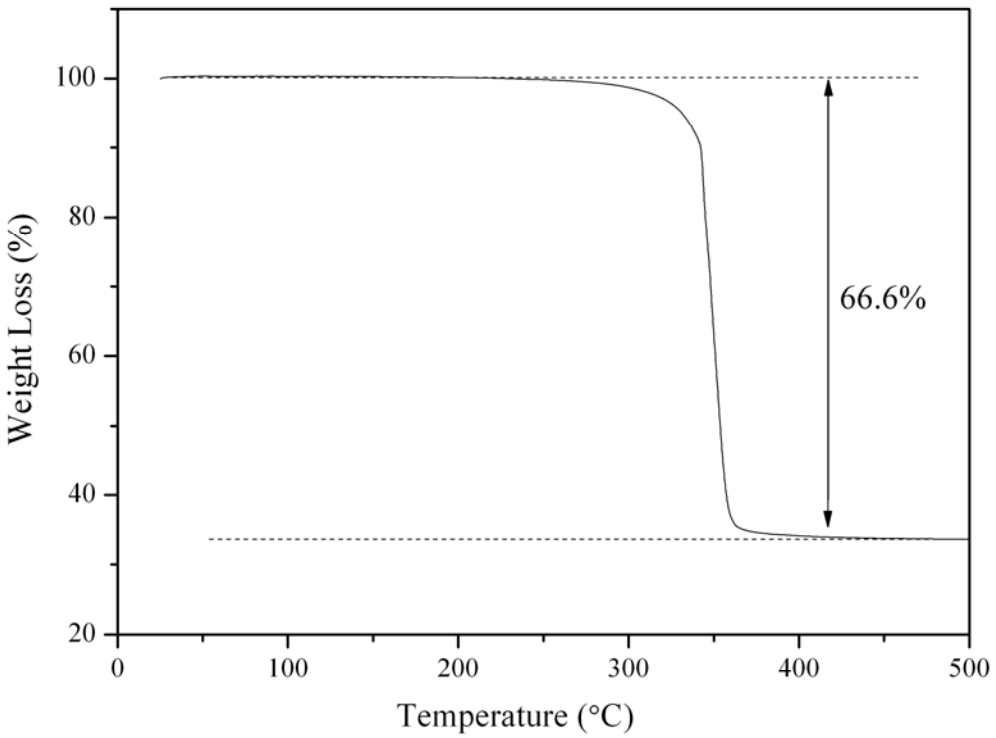

Figure 8. Weight loss as a function of temperature for the powdered perovskite *MA*PbI_3. Thermogravimetic analysis was performed at a rate of 5°C/min under an argon atmosphere.

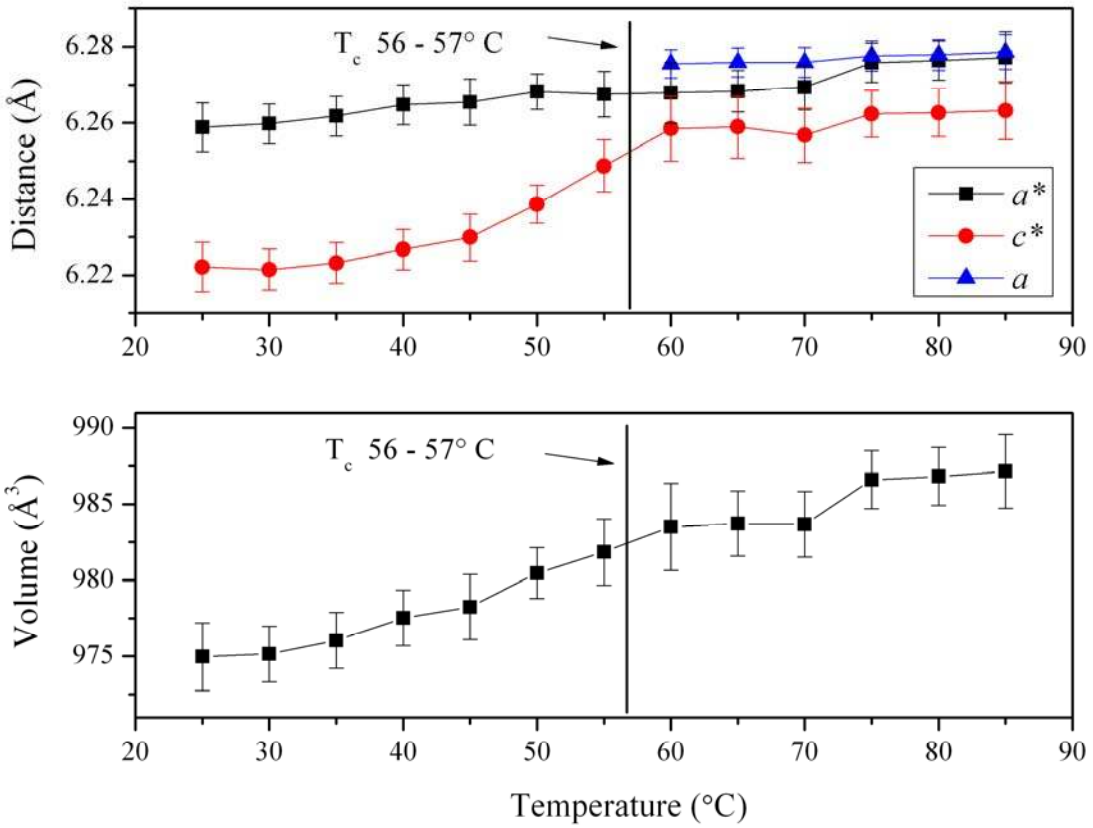

Figure 9. Plot of the lattice parameters and cell volume derived from the variable temperature powder X-ray diffraction experiments. The tetragonal lattice parameters were first converted to their pseudo-cubic parameters using the relation $a^* = a_{tet}/\sqrt{2}$ and $c^* = c_{tet}/2$.

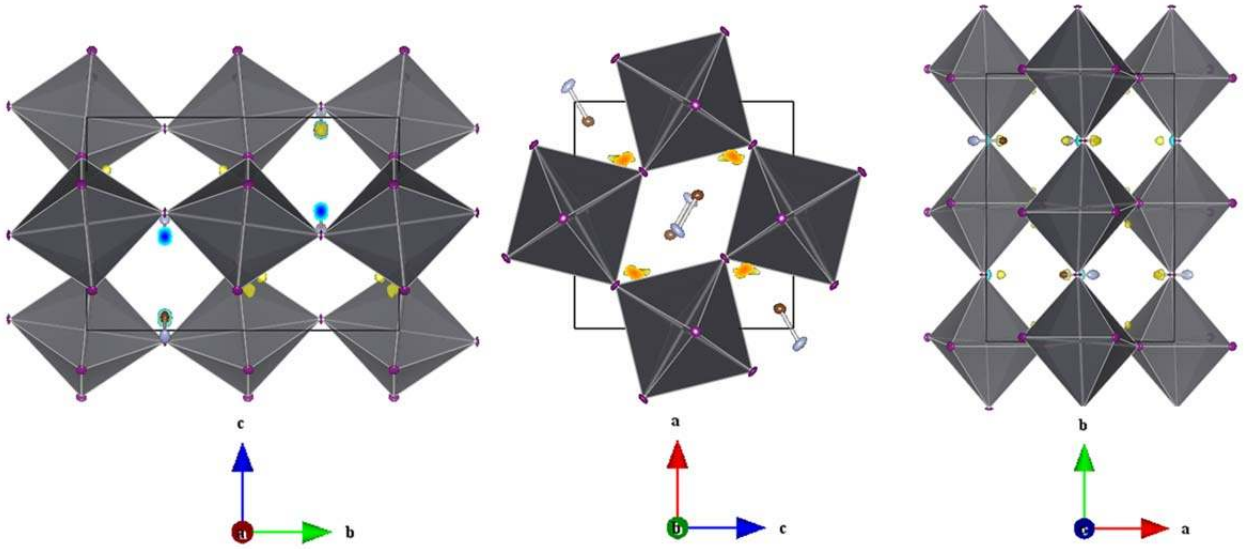

Figure 10. 3D difference Fourier maps showing the regions of positive (yellow) and negative (blue) electron densities (regions indicated > ±5 electrons) when viewed along the *a*, *b* and *c* directions of orthorhombic structure of *MA*PbI_3 respectively.

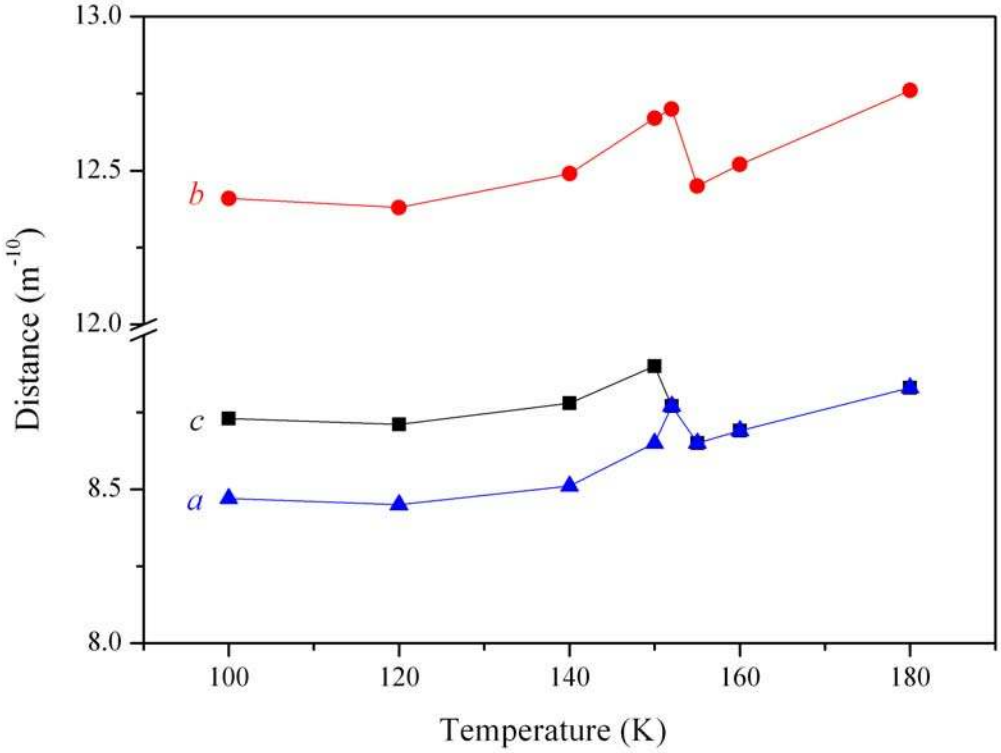

Figure 11. Low temperature variation in lattice parameters for *MA*PbI_3 determined using single-crystal XRD. The discontinuity correlates with the reported orthorhombic to tetragonal transition.

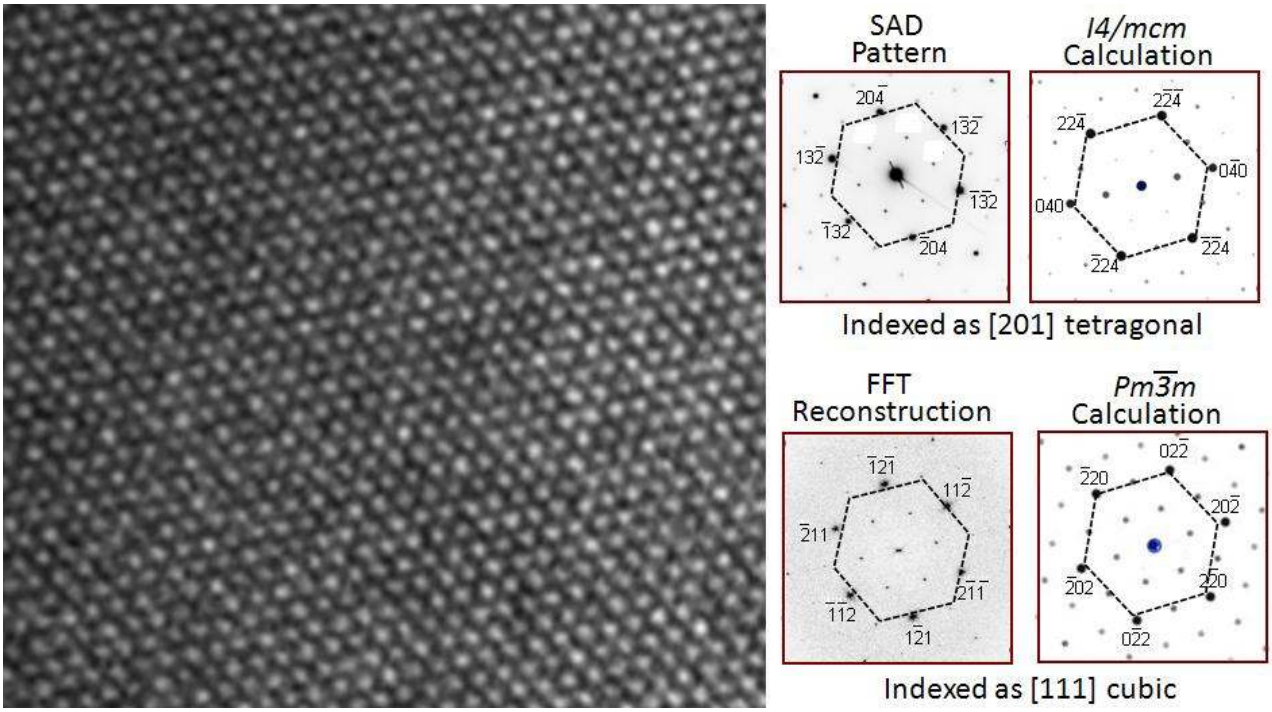

Figure 12. A high resolution phase contrast image $[201]_t \equiv [111]_c$ of *MA*PbI_3 shows translational order. The SAD pattern and inverse FFT of the image yield similar periodicities that while metrically consistent with cubic or tetragonal cells, show intensities that disagree with 2-beam and multi-beam diffraction simulation in both *I*4/*mcm* and *Pm*-3*m*. In particular, for the RT I4/mcm phase the {13-2}/{20-4} reflections are intense but computation shows the most intense reflection to be {040}/{2-24}. The origin of the differences is not due to crystal thickness or beam divergence effects and requires further investigation.

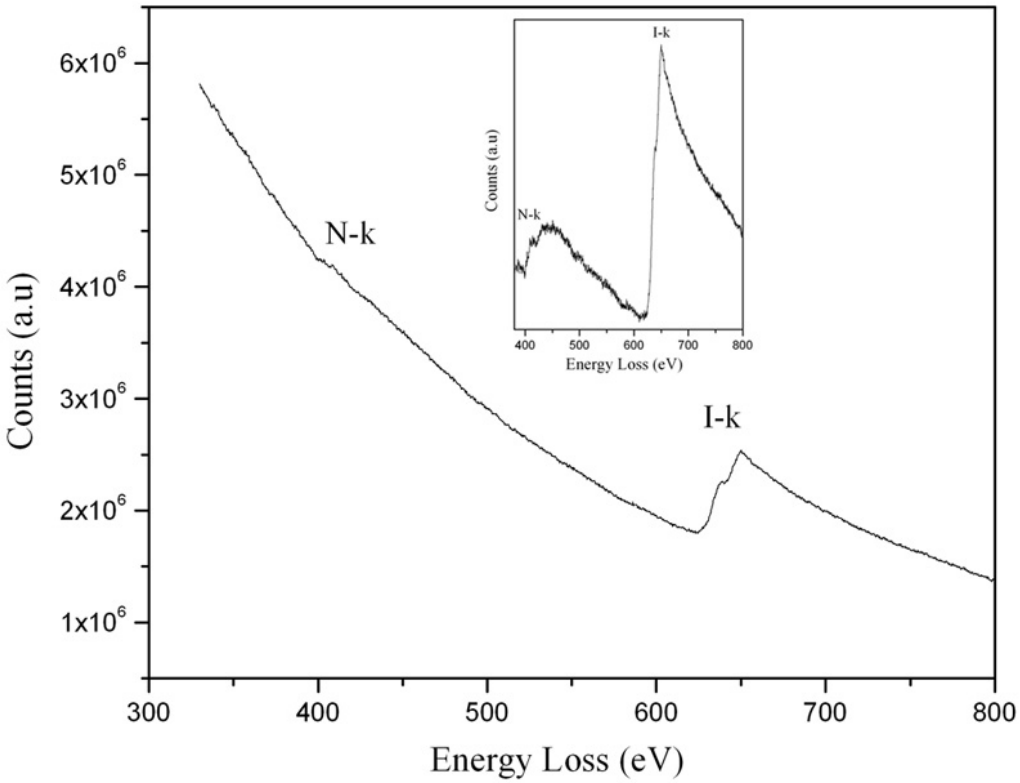

Figure 13. EELS spectra of *MA*PbI_3 powders showing the N and I *K*-shell ionisation edges superimposed on a decreasing background arising from multiple inelastic scattering.

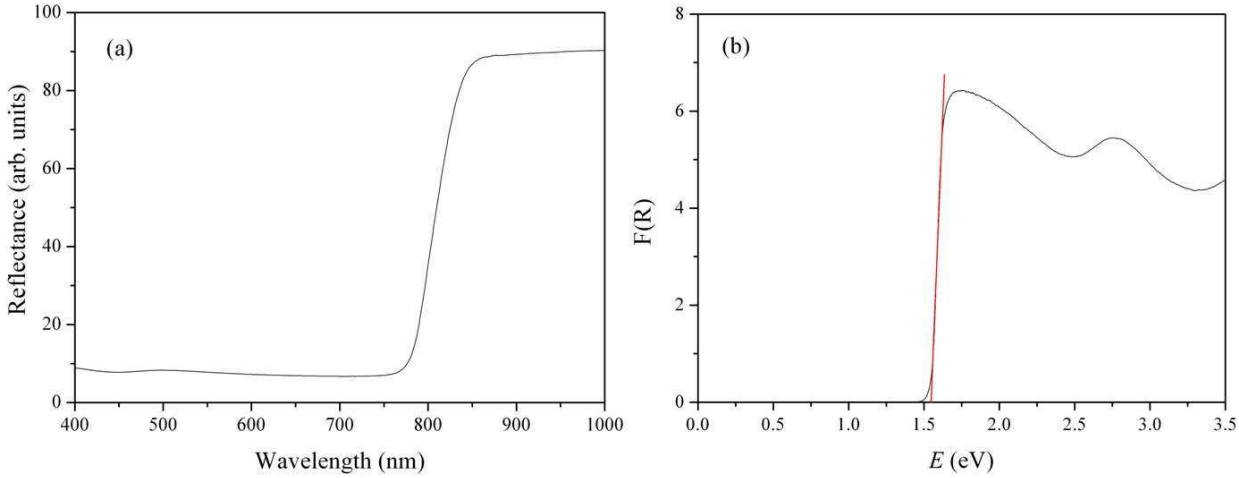

Figure 14. (a) Diffuse reflectance spectra for *MA*PbI_3, (b) The Kubelka-Munk spectrum for *MA*PbI_3 revealing a band gap *E*g = 1.51eV.

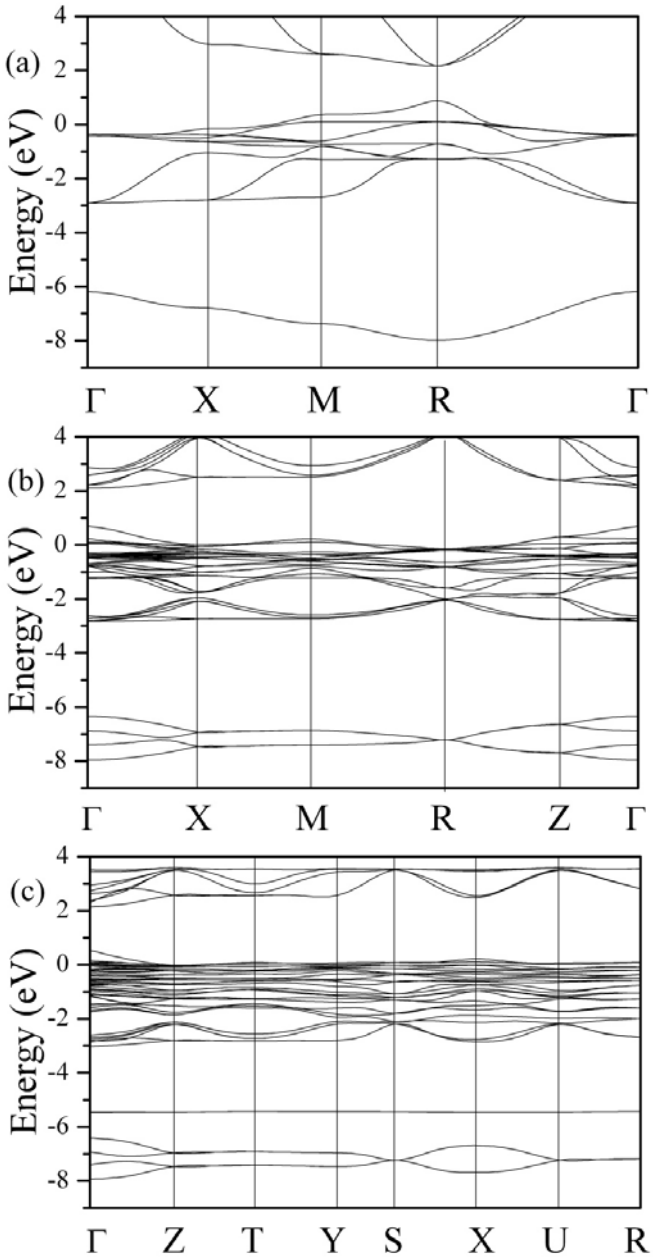

Figure 15. Calculated band structures of (a) cubic, (b) tetragonal, and (c) orthorhombic phases of *MA*PbI_3 along the high-symmetry lines in the first Brillouin zone.

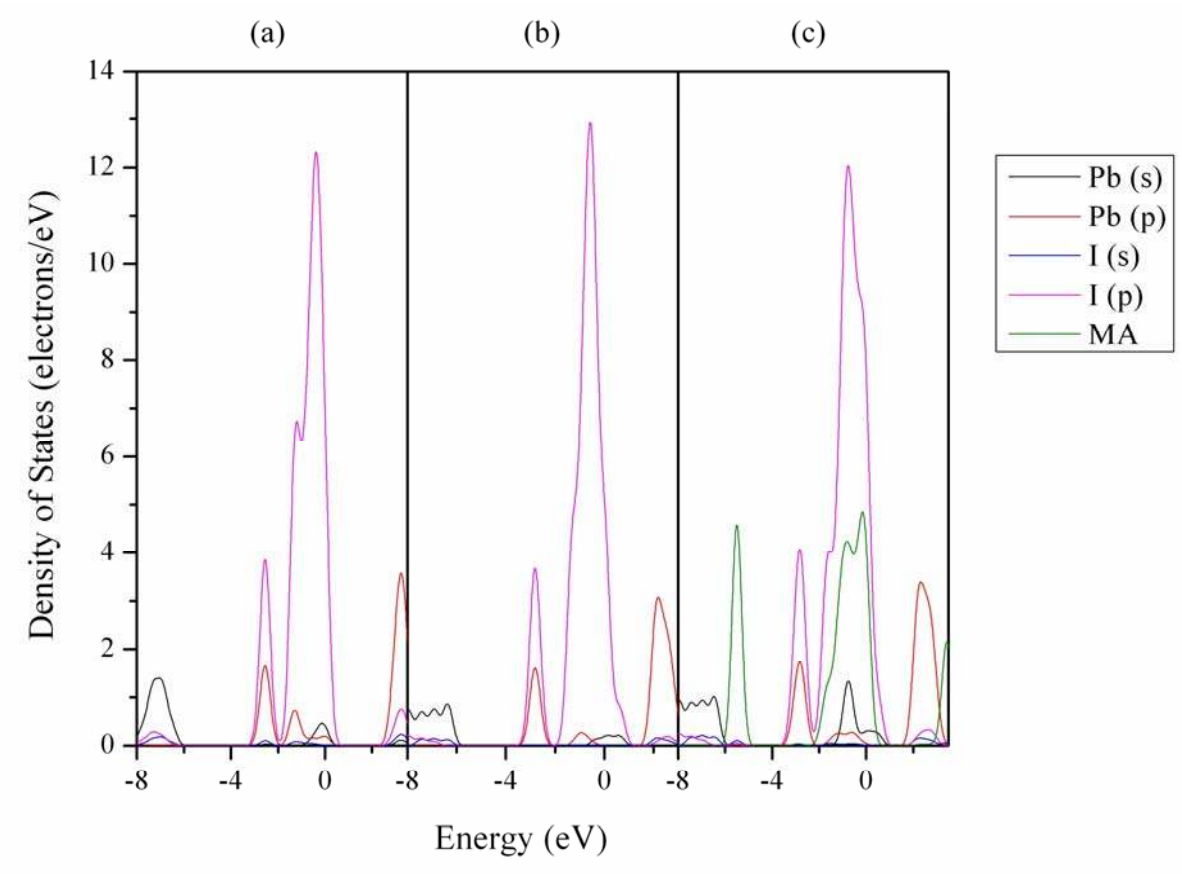

Figure 16. PDOS on (a) Pb *s, p* and I *s, p* orbitals of cubic phase and (b) tetragonal phase; (c) MA (all orbitals), Pb *s, p* and I *s, p* orbitals of orthorhombic phase.

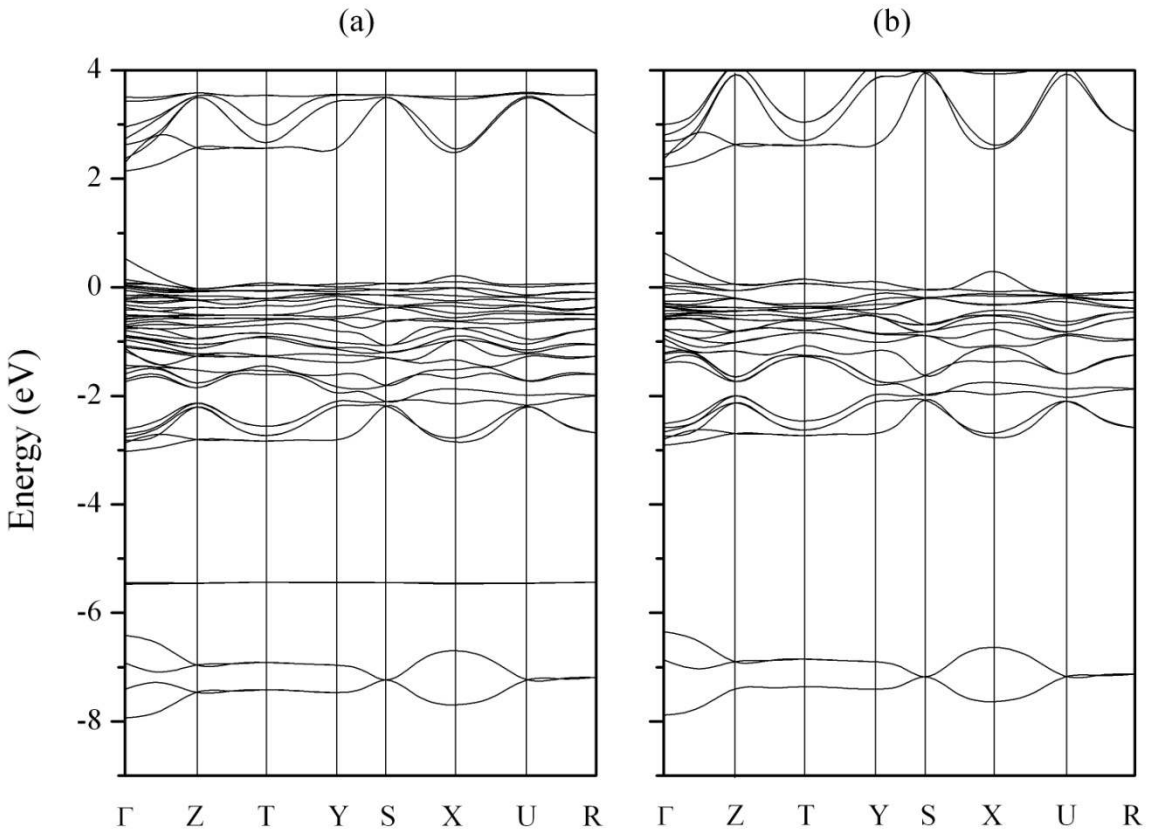

Figure 17. Calculated band structures of orthorhombic *Pnma* phase with (a) and without (b) the *MA* group.

Table 1. Reported phase transformations for $CsSnI_3$ upon heating.

Phase	**III**	**II**	**I**
Temperature/K	300K	350	478
Space Group	*Pnma (62)*	*P*4/*mbm* (No. 127)	*Pm*-3*m* (No. 221)
Crystal System	Orthorhombic	Tetragonal	Cubic
Z	4	2	1
Lattice Parameters	*a* = 8.6885(5) Å *b* = 12.3775(4) Å *c* = 8.6384(6) Å	*a* = 8.7182(8) Å *c* = 6.1908(6) Å	*a* = 6.2057(7) Å

Table 2. Reported phase transformations for *MA*$GeCl_3$ upon heating.

Phase	**IV**	**III**	**II**	**I**
Temperature/K	2	250	370	475
Space Group	$P2_1/n$ (No.14)	*Pnma* (No. 62)	*R*3*m* (No.160)	*Pm*-3*m* (No. 221)
Crystal System	Monoclinic	Orthorhombic	Trigonal	Cubic
Z	4	4	1	1
Lattice Parameters	a = 10.9973(1) Å b = 7.2043(1) Å c = 8.2911(1) Å α = 90.470(1)°	a = 11.1567(1) Å b = 7.3601(1) Å c = 8.2936(1) Å	a = 5.6784(1) Å α = 90.945(1)°	a = 5.6917(2) Å

Table 3. Reported phase transformations for *MA*$SnBr_3$ upon heating.

Phase	**IV**	**III**	**II**	**I**
Temperature/K	297	318	350	478
Space Group	*P*1 (No.1)	*Pc* (No. 7)	*R*3*m* (No.160)	*Pm*-3*m* (No. 221)
Crystal System	Triclinic	Monoclinic	Trigonal	Cubic
Z	4	4	1	1
Lattice Parameters	a = 5.726 Å b = 8.227 Å c = 7.910 Å α = 90.40° β = 93.08° γ = 90.15°	a = 5.718(1) Å b = 8.236(1) Å c = 7.938(1) Å β = 93.03(1)°	a = 5.734(1) Å α = 91.90(1)°	a = 5.760(1) Å

Table 4. Refined lattice parameters for *MA*PbI_3 derived from the variable temperature powder X-ray diffraction experiments

	Tetragonal			**Cubic**	
Temperature (°C)	***a* (Å)**	***c* (Å)**	***Vol* (Å^3)**	***a* (Å)**	***Vol* (Å^3)**
25	8.851(9)	12.444(13)	975.0(2.2)	-	-
30	8.853(7)	12.443(11)	975.1(1.8)	-	-
35	8.855(7)	12.446(11)	976.0(1.8)	-	-
40	8.860(7)	12.453(11)	977.5(1.8)	-	-
45	8.861(9)	12.460(12)	978.2(2.1)	-	-
50	8.865(7)	12.477(10)	980.5(1.7)	-	-
55	8.864(9)	12.497(14)	981.8(2.2)	-	-
60	8.864(11)	12.517(17)	983.5(2.9)	6.276(4)	247.1(0.4)
65	8.865(8)	12.518(16)	983.7(2.1)	6.276(4)	247.2(0.4)
70	8.866(8)	12.513(14)	983.7(2.2)	6.276(4)	247.2(0.5)
75	8.875(7)	12.525(12)	986.6(1.9)	6.278(4)	247.4(0.5)
80	8.876(7)	12.525(12)	986.8(1.9)	6.278(4)	247.4(0.5)

85	8.877(9)	15.526(15)	987.1(2.5)	6.279(5)	247.5(0.5)

Table 5. Pseudo-cubic lattice parameters calculated from the refined tetragonal supercell.

Temperature (°C)	$a^* = a_{tet}/\sqrt{2}$	$c^* = c_{tet}/2$
25	6.2588	6.2222
30	6.2597	6.2215
35	6.2617	6.2232
40	6.2647	6.2267
45	6.2655	6.2299
50	6.2682	6.2386
55	6.2675	6.2487
60	6.2679	6.2585
65	6.2683	6.2590
70	6.2694	6.2567
75	6.2758	6.2623
80	6.2764	6.2626
85	6.2771	6.2632

Table 6. Refinement details for the single crystal data of orthorhombic *MA*PbI_3

Crystal size	0.1 × 0.1 × 0.1 mm
Crystal system	Orthorhombic
Space group	*Pnma* (No. 62)
Temperature	100K
Unit cell dimensions	
a (Å)	8.8362(11)
b (Å)	12.5804(15)
c (Å)	8.5551(10)
V ($Å^3$)	951.01
Z	4
Density (g cm^{-3})	4.2864
μ (cm^{-1})	27.39
Radiation Mo $K\alpha$ (Å)	0.71069
Collection limits (θ, deg)	2.88 – 32.08
Data measured	17319
Unique reflections	1731
Reflections with $I \geq 3\sigma(I)$	1344
R	0.0523
R_W	0.1299
GOF	2.48
D residual (e$Å^{-3}$)	

+	6.55
-	-9.11

Table 7. Refined atomic position and atomic displacement parameters for orthorhombic (*Pnam*) *MA*PbI_3.

Site	*x*	*y*	*z*	U_{Iso}
Pb	0.5	0	0	0.00608(16)
I1	0.48572(11)	0.25	-0.05291(14)	0.0130(3)
I2	0.19020(9)	0.01719(6)	0.18615(10)	0.0168(2)
N	0.932(2)	0.75	0.029(2)	0.030(5)
C	0.913(2)	0.25	0.061(2)	0.019(5)

	U_{11}	U_{22}	U_{33}	U_{12}	U_{13}	U_{23}
Pb1	0.0068(3)	0.0028(3)	0.0086(3)	0.00005(16)	0.00011(18)	0.00028(18)
I1	0.0187(5)	0.0021(4)	0.0183(6)	0	0.0021(4)	0
I2	0.0157(4)	0.0206(4)	0.0143(4)	0.0013(3)	0.0092(3)	0.0009(3)
N	0.035(10)	0.023(9)	0.033(10)	0	0.020(8)	0
C	0.019(8)	0.011(8)	0.027(10)	0	-0.002(8)	0

Table 8. Lattice parameters determined from the low temperature single crystal X-ray diffraction experiments.

	Lattice Parameters (Å)		
T (K)	***a***	***b***	***c***
100	8.73(9)	12.41(13)	8.47(9)
120	8.71(8)	12.38(11)	8.45(7)
140	8.78(6)	12.49(9)	8.51(6)
150	8.90(5)	12.67(7)	8.65(5)
152	8.77(5)	12.70(8)	8.77(5)
155	8.65(7)	12.45(10)	8.65(7)
160	8.69(6)	12.52(9)	8.69(6)
180	8.83(3)	12.76(4)	8.83(3)

References

1. J. H. Im, C. R. Lee, J. W. Lee, S. W. Park and N. G. Park, *Nanoscale*, 2011, **3**, 4088-4093.
2. H. S. Kim, C. R. Lee, J. H. Im, K. B. Lee, T. Moehl, A. Marchioro, S. J. Moon, R. Humphry-Baker, J. H. Yum, J. E. Moser, M. Grätzel and N. G. Park, *Scientific Reports*, 2012, **2:591**, DOI: 10.1038/srep00591.
3. M. M. Lee, J. Teuscher, T. Miyasaka, T. N. Murakami and S. H. J, *Science*, 2012, **338**, 643-647.
4. A. M. Glazer, *Acta. Crystallogr. B*, 1972, **28**, 3384-3392.
5. A. M. Glazer, *Acta. Crystallogr. A*, 1975, **31**, 756-762.

6. C. J. Howard and H. T. Stokes, *Acta. Crystallogr. A*, 1998, **54**, 782-789.
7. I. P. Swainson, *Acta. Crystallogr. B*, 2005, **61**, 616-626.
8. C. K. Møller, *Nature*, 1957, **180**, 981-982.
9. C. K. Møller, *Nature*, 1958, **182**, 1436.
10. H. Mashiyama, Y. Kurihara and T. Azetzu, *J. Kor. Phys. Soc*, 1998, **32**, S156-S158.
11. Y. Kawamura and H. Mashiyama, *J. Kor. Phys. Soc*, 1999, **35**, S1437-S1440.
12. K. Fütterer, W. Depmeier and V. Petricek, *Acta Cryst.* , 1995, **B51**, 768-779.
13. D. Weber, *Z. Naturforsch*, 1978, **33b**, 1443-1445.
14. D. B. Mitzi, S. Wang, C. A. Feild, C. A. Chess and A. M. Guloy, *Science*, 1995, **267**, 1473-1476.
15. D. B. Mitzi, *J. Chem. Soc., Dalton Trans.*, 2001, 1-12.
16. S. J. Clark, J. D. Donaldson and J. A. Harvey, *J. Mater. Chem.*, 1995, **5**, 1813-1818.
17. I. Chung, J. H. Song, J. Im, J. Androulakis, C. D. Malliakas, H. Li, A. J. Freeman, J. T. Kenney and M. G. Kanatzidis, *J. Am. Chem. Soc.*, 2012, **134**, 8579-8587.
18. K. Yamada, S. Funabiki, H. Horimoto, T. Martsui, T. Okuda and S. Ichiba, *Chem. Lett.*, 1991, 801-804.
19. I. Chung, B. Lee, J. He, R. P. H. Chang and M. G. Kanatzidis, *Nature*, 2012, **485**, 486-490.
20. A. N. Christensen and S. E. Rasmussen, *Acta Chem. Scand.*, 1965, **19**, 421-428.
21. B. Winkler, V. Milman and M. H. Lee, *J. Chem. Phys.*, 1998, **108**, 5506-5509.
22. W. Depmeier, A. Möller and K. H. Klaska, *Acta. Crystallogr. B*, 1980, **36**, 803-807.
23. K. Yamada, K. Isobe, E. Tsuyama, T. Okuda and Y. Furukawa, *Solid State Ionics*, 1995, **79**, 152-157.
24. K. Yamada, K. Isobe, T. Okuda and Y. Furukawa, *Z. Naturforsch. A*, 1994, **49**, 258-266.
25. T. Okuda, S. Gotou, T. Takahashi, H. Terao and K. Yamada, *Z. Naturforsch.* , 1996, **51**, 686-692.
26. K. Yamada, K. Mikawa, T. Okuda and K. S. Knight, *J. Chem. Soc., Dalton Trans.*, 2002, 2112-2118.
27. K. Yamada, Y. Kuranaga, K. Ueda, S. Goto, T. Okuda and Y. Furukawa, *Bull. Chem. Soc. Jpn.*, 1998, **71**, 127-134.
28. N. Onoda-Yamamuro, O. Yamamuro, T. Matsuo, H. Suga, K. Oikawa, N. Tsuchiya, T. Kamiyama and H. Asano, *Physica B*, 1995, **213-214**, 411-413.
29. I. P. Swainson, L. Chi, J. H. Her, P. S. Cranswick, B. Winkler, D. J. Wilson and V. Milman, *Acta. Crystallogr. B*, 2010, **66**, 422-429.
30. M. Mori and H. Saito, *J. Phys. C: Solid State Phys.*, 1986, **19**, 2391-2401.
31. H. Mashiyama, Y. Kawamura, H. Kasano, T. Asahi, Y. Noda and H. Kimura, *Ferroelectrics*, 2007, **348**, 182-186.
32. I. P. Swainson, R. P. Hammond, C. Soulliére, O. Knop and W. Massa, *J. Solid State Chem.*, 2003, **176**, 97-104.
33. A. Poglitsch and D. Weber, *J. Chem. Phys.*, 1987, **87**, 6373-6378.
34. I. P. Swainson, M. G. Tucker, D. J. Wilson, B. Winkler and V. Milman, *Chem. Mater.*, 2007, **19**, 2401-2405.
35. R. E. Wasylishen, O. Knop and J. B. Macdonald, *Solid state Commun.*, 1985, **56**, 581-582.
36. Y. Kawamura, H. Mashiyama and K. Hasebe, *J. Phys. Soc. Jpn.*, 2002, **71**, 1694-1697.
37. N. Onoda-Yamamuro, T. Matsuo and H. Suga, *J. Phys. Chem. Solids*, 1990, **51**, 1383-1395.
38. N. Onoda-Yamamuro, T. Matsuo and H. Suga, *J. Phys. Chem. Solids*, 1992, **53**, 935-939.
39. B. R. Vincent, K. N. Robertson, T. S. Cameron and K. Osvald, *Can. J. Chem.*, 1987, **65**, 1042-1046.
40. Bruker, *Topas Version 4.1*, (2008) Bruker AXS Inc., Madison, Wisconsin, USA.
41. R. W. Cheary and A. Coelho, *J. Appl. Crystallogr.*, 1992, **25**, 109-121.
42. R. W. Cheary and A. Coelho, *J. Appl. Crystallogr.*, 1998, **31**, 851-861.
43. D. Hyde, *Graph software for scientists and engineers (available at www.dplot.com)*, (2012).

44. V. Petriček, M. Dusek and L. Palatinus, *Jana2006. The crystallographic computing system.*, (2006), Institute of Physics, Praha, Czech Republic.
45. L. Palatinus and G. Chapuis, *J. Appl. Crystallogr.*, 2007, **40**, 786-790.
46. K. Momma and F. Izumi, *J. Appl. Cryst.*, 2008, **41**, 653-658.
47. P. Stadelmann, *JEMS, 12M-EPFL, CH-1015*, (2003), Switzerland.
48. W. Kohn and L. J. Sham, *Phys. Rev.*, 1965, **140**, 1133.
49. J. P. Perdew, K. Burke and M. Ernzerhof, *Phys. Rev. Lett.*, 1996, **77**, 3865.
50. M. Segall, P. Linda, M. Probert, C. Pickard, P. Hasnip, S. Clark and M. Payne, *Materials Studio CASTEP Version 2.2*, (2002).
51. Y. Takahashi, R. Obara, Z. Z. Lin, Y. Takahashi, T. Naito, T. Inabe, S. Ishibashi and K. Terakura, *Dalton Trans.*, 2011, **40**, 5563-5568.
52. J. Chabot, M. Côté and J. Bri'ere, American Physical Society, March Meeting, 2004.
53. D. B. Mitzi, C. A. Feild, W. T. A. Harrison and A. M. Guloy, *Nature*, 1994, **369**, 467.
54. D. B. Mitzi, *Prog. Inorg. Chem.*, 1999, **48**, 1.
55. I. Borriello, G. Cantele and D. Ninno, *Phys. Rev. B*, 2008, **77**, 235214.
56. V. Krämer and E. Post, *Mat. Res. Bull.*, 1985, **20**, 407-412.
57. K. Gesi, *Ferroelectrics*, 1997, **203**, 249.
58. M. Sakata, J. Harada, M. J. Cooper and K. D. Rouse, *Acta Cryst. A*, 1980, **36**, 7-15.
59. R. J. Worhatch, H. S. Kim, I. P. Swainson, A. L. Yonken and S. J. L. Billinge, *Chem. Mater.*, 2008, **20**, 1272-1277.
60. J. Torrent and V. Barron, *Encyclopedia of Surface and Colloid Science*, Marcel Dekker, Inc, New York, 2002.
61. T. Umebayashi and K. Asai, *Phys. Rev. B*, 2003, **67**, 155405.